Journal of Materials Chemistry A

Accepted Manuscript

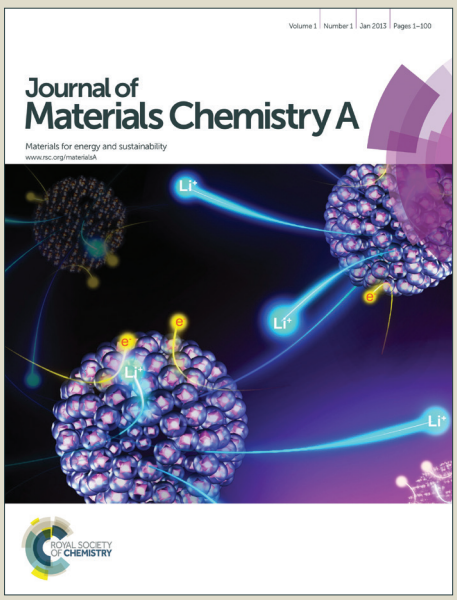

ROYAL SOCIETY OF CHEMISTRY

www.rsc.org/materialsA

Hybrid MnO_2/C nano-composites on macroporous electrically conductive network for supercapacitor electrodes

Dajun Wu[a], Shaohui Xu[a], Mai Li[a], Chi Zhang[a], Yiping Zhu[a], Yuwei Xu [a], Weiwei Zhang[a], Rong Huang[a], Ruijuan Qi[a], Lianwei Wang[a,b*], Paul K. Chu[b]

[a] Key Laboratory of Polar Materials and Devices, Ministry of Education, and Department of Electronic Engineering, East China Normal University, 500 Dongchuan Road, Shanghai 200241, P. R. China

[b] Department of Physics and Material Science, City University of Hong Kong, Tat Chee Avenue, Kowloon, Hong Kong, China

*** Corresponding author:** LW Wang (Tel: +86-021-54345160; Fax: +86-021-54345119; Email: lwwang@ee.ecnu.edu.cn)

Abstract

A two-step hydrothermal process is designed to synthesize hybrid MnO_2/C nano-composites on a macroporous electrically conductive network (MECN) *via* a redox reaction in a 30 mM $KMnO_4$ solution with carbon microspheres. The microstructure, surface morphology, and electrochemical properties of the MnO_2/C coated on MECN are determined systematically. The MnO_2 nanoflakes, which are about 40-200 nm, are deposited regularly on the carbon microspheres coated on the

MECN electrode. The MnO_2 nano-lamellas offer fast ion transport and adsorption-desorption to/from the MnO_2 surface, and the microporous carbon microspheres enhance the electrical storage and ion transfer. The *in situ* growth of MnO_2 on the carbon microspheres on a MECN substrate leads to a small contact resistance and short current transfer length. The materials are demonstrated to be excellent electrodes in supercapacitors boasting a high capacitance of 497 F/g at 1 A/g with 1 cm^2 electrode and excellent long-term cycling stability over 5,000 cycles in 1 M Na_2SO_4. The MnO_2/C/MECN||active carbon/Ni-foam asymmetrical supercapacitors (ASCs) deliver an energy density of 0.50 mW h cm^{-3} (55.5 Wh kg^{-1} at a power density of 4,000 W kg^{-1}) with 87.6% retention of the specific capacitance after 5,000 cycles.

1. INTRODUCTION

In order to meet the increasing demand for energy conversion and storage equipment such as portable electronic products and (hybrid) electrical vehicles, supercapacitors have attracted a lot of attention.[1, 2] Owing to advantages like long cycling life, outstanding power density, fast charging-discharging rate, environmentally friendly, and good safety, supercapacitors may replace low-power batteries in the future.[3-6] In general, supercapacitors can be categorized into electrical double layer capacitors (EDLCs) and faradic pseudo-capacitors according to the energy storage reaction mechanism.[7, 8] In EDLCs, the capacitance depends on rapid accumulation of electrostatic charges at the interface of the electrode/electrolyte such as active carbon, carbon nanotubes (CNT), and reduced graphene oxide (rGO),[9-11] whereas in pseudo-capacitors, energy storage involves the reversible and fast faradic redox reaction between the surface electroactive materials and electrolyte such as metal oxides (RuO_2, MnO_2, NiO, Co_3O_4, Fe_3O_4, SnO_2, etc.), hydroxides ($Ni(OH)_2$, $Co(OH)_2$, etc.), and conducting polymers (polyaniline (PPA), polypyrrole (PPR) and polythiophene (PTE)).[12-20] In general, microporous carbon materials with a large surface area and good conductivity are utilized in EDLCs as the negative electrode and have good stability and low specific capacitance. In comparison, pseudo-capacitors have high specific capacitance but relatively low charging-discharging rate and unsatisfactory stability.[20] Hence, micro/nano-composite architectures formed by active carbon (e.g. microporous carbon microspheres) and metal oxides (e.g. MnO_2) as binary or ternary electro-active materials integrate the

advantages of EDLCs active materials and pseudo-capacitive electro-active materials leading to good special capacitance, charging-discharging rates, and cycling lifetime.[21-23] Among the various transition-metal oxides, manganese oxides (MnO,[24, 25] MnO_2,[12-20] Mn_3O_4[26-29] and Mn_2O_3[30, 31]) are promising in electrochemical capacitor electrodes because of the low cost, high theoretical capacitance (~1370 F g^{-1}), and non-toxicity. In particular, MnO_2 has a high specific theoretical capacity (~1232 F g^{-1}) as a pseudo-capacitor electrode material and excellent electrochemical characteristics. However, practical adoption of pure MnO_2 is hampered by the poor conductivity (~10^{-5} S cm^{-1}), [32] low ion adsorption/desorption constant. And we also meet the problem of Mn dissolution into the electrolyte.[33]

To overcome the hurdles associated with the low electrical conductivity and ion diffusion, three approaches have been proposed. The first is to synthesize MnO_2 nano-structures with a uniform morphology and large specific surface area to shorten the ion and electron diffusion length. Various nano-scale structures of MnO_2, including nanorods,[34] nanowires,[35] nanotubes,[36] nanobelts,[37] and nanoflowers,[38] have been explored to improve the electrochemical performance of MnO_2-based supercapacitors. For instance, Yu et al. reported a simple hydrothermal method to produce urchin- and clew-like nanostructures without using any template and surfactant and the materials showed a specific capacity of 120F g^{-1} at a scanning rate of 5 mVs^{-1} in a 1 M Na_2SO_4 aqueous electrolyte solution.[39] Qu et al. described a precipitation reaction to produce MnO_2 nanorods with a capacitance of 201 F/g and excellent cycling behavior in the Li_2SO_4 electrolyte.[34] Brousse and co-workers

synthesized and investigated various MnO_2 compounds and showed that the 2D structure of birnessite had a high specific capacitance of 110F/g and surface area of $17m^2/g$.[40] The second method is to fabricate nanocomposites with a carbon substrate (e.g. carbon microspheres, carbon nanotube (CNT), graphene, graphene oxide) as the electrode. It combines the merits of carbon and MnO_2 nanomaterials to enhance the electrical conductivity.[41] He et al. produced flexible 3D graphene supported MnO_2 supercapacitor by electrodeposition and the materials possessed a high area capacitance of $1.42F/cm^2$ at 2mV/s and highest specific capacitance of 130F/g.[42] Zhang et al. prepared a MnO_2/active carbon supercapacitor by an oxidation-reduction reaction using potassium permanganate and active carbon.[43] Ma and co-workers prepared thin MnO_2 nanosheets on CNT with a uniform morphology by a hydrothermal reaction involving $KMnO_4$ and CNTs.[44] The third method is to construct hollow or porous micro/nanostructures with a large surface area and plenty of active sites to enhance the specific capacitance and power density by developing a deep electrode/electrolyte contact area and accommodating larger-volume change.[45] For instance, Zhang et al. synthesized a core-shell MnO_2-MnO_2/C nanocomposite by a two-step hydrothermal method and the materials had high specific energy and power densities.[46] Li and co-workers prepared mesoporous carbon microspheres by simple thermal decomposition and a maximum specific energy and energy density of 164 Wh/kg and 25 kWh/L, respectively, were obtained.[47] Based on these results, if the MnO_2 nanostructure can be uniformly embedded into a carbon coat on a conductive substrate and the thickness and morphology of the MnO_2/C nano-composites can be

controlled, they can be excellent supercapacitor materials. In fact, various carbon microspheres have been synthesized using different carbon sources such as glucose[46], microalgaes[25], and polymers.[4, 6]

In our previous study, we demonstrated the production of a MnO_2 macroporous electrically conductive network (MECN) by one-step electroplating as a miniature supercapacitor.[48] The unique structure of MECN not only introduce robustness and durability, but also preserve the structure of the substrate in the Na_2SO_4 electrolyte leading to good performance as a miniature supercapacitor. However, the big resistance between the MECN and MnO_2 nanosheets result in an inferior charging-discharging performance. Hence, carbon mcirospheres are embedded to reduce the resistance between the MECN substrate and MnO_2 nanosheets. MECNs have been fabricated by our research team using a micro-electromechanical system (MEMS) process and electro-deposition.[49] Herein, we describe the hydrothermal synthesis of MECN supported hybrid MnO_2/C hierarchical nano-composites and evaluate the performance as supercapacitor electrode materials.

2. Experimental details

2.1 Chemicals and materials

All of the chemical reagents were analytical grade and used without further purification. Nickel chloride ($NiCl_2 \cdot 6H_2O$), D-glucose, ammonium chloride (NH_4Cl), and potassium permanganate ($KMnO_4$) were purchased from Aladdin Reagent. Sodium hypophosphite ($NaH_2PO_2 \cdot H_2O$), ethanol, acetone, and the other reagents were

obtained from Sinopharm Chemical Reagent Co. Ltd. Deionized water (18 MΩ) was used in all the experiments. The Si microchannel plates (Si-MCP) were fabricated by electrochemical etching[49] and divided into 1 cm × 1 cm samples by laser cutting.

2.2 Preparation of the MECN

The MECNs were synthesized by the electroless process of nickel or copper (nickel in this paper) onto silicon microchannel plate by our patented method called flowing deposition, and then followed by electroplating.[48, 49, 69, 70] The silicon microchannel plate composed square array of with 5×5 μm pores arrays channels about 200 μm in depth and 1 μm thickness of wall, The intrinsic resistance is on the order of kΩ. The nickel layer was deposited on both the outer surface and inner side walls of the Si-MCPs at the same time. In order to decrease the electrical resistivity, additional nickel was deposited on the samples by electroplating in a standard plating bath at room temperature in an electrolyte of 0.1 M $NiCl_2$ and 2 M NH_4Cl at a pH of 3. The distance of the working and counter electrodes, namely MECN and Pt foil, respectively, was 1 cm and a small current density of 0.1A/cm^2 was applied for 100 s.

2.3 Preparation of the C/MECN and synthesis of the nano-flake MnO_2/C/MECN

The synthesis of C/ MECN and MnO_2/C/ MECN is schematically illustrated in Fig. 1. Firstly, nickel was deposited on the Si-MCPs to form the MECN as the current collector by electroless plating and electro-deposition. Subsequently, the mixture were formed by dissolving 0.3 g of glucose in 20 ml of deionized water and stirred for 30 min. The as-prepared MECN was immersed in the 0.1% Triton X100 solution for 5 min and introduced into the above solution. The solvent was transferred and tightly

sealed in a 25 ml the Teflon-sealed stainless steel autoclave, keeping the autoclave at 180℃ for 6 to 24 h; the C/MECN was formed. Afterwards, the autoclave was allowed to cool down naturally. The glucose was dehydrated and polymerized to form oligosaccharides under hydrothermal conditions.[50] A lot of the oligosaccharide molecules might be inserted into the inside and surface of the MECN (Fig.1). The oligosaccharides underwent intermolecular dehydration, cross-linking, and carbonization to form colloidal carbonaceous spheres as the aromatization reaction products.[51] The colloidal carbonaceous microspheres in the MECN samples were further carbonized by calcinations at 800℃ for 2 h under flowing argon at a rate of 100 sccm. The initial amorphous structures were preserved because the annealing temperature was lower than the graphitizing temperature of about 3000 ℃. Afterwards, MnO_2 was fabricated and coated on the surface of the C/MECN samples by a hydrothermal process with $KMnO_4$ being the precursor. The redox reaction between MnO_4^- and carbon resulted in spontaneous reduction of MnO_4^- to MnO_2 on the surface and sidewall of the C/ MECN as shown in the following:[37, 52]

$$4MnO_4^- + 3C + H_2O \rightarrow 4MnO_2 + CO_3^{2-} + 2HCO_3^- . \quad (1)$$

MnO_2 was *in situ* uniformly loaded on the surface of C/MECN.

The experiments were performed as following. The C/MECN samples were immersed in 100 ml of 30 mM $KMnO_4$ aqueous solution under vigorous stirring. The replacement reaction was performed in a 60 ℃ water bath hydrothermally for 8 to 24 h. The samples were cleaned and dried in a vacuum oven at 60 ℃ overnight and the mass of the MnO_2/C of MnO_2/C/MECN was about 3 mg/cm^2.

2.4 Preparation of the active carbon/Ni-foam

The active carbon (AC)/Ni-foam electrodes were fabricated by the process described previously.[6] Briefly, the active carbon (about 6.6 mg/cm^2) (80 wt%), acetylene black (10 wt%), and polytetrafluoroethylene suspension (10 wt%) were mixed and ultrasonic dispersed in isopropanol to obtain a homogeneous slurry. The mixture was uniformly put on the nickel foam substrate (1 cm × 1 cm) dropwisely, dried at 90 ℃, and then dried at 60 ℃ in a vacuum oven overnight to produce the electrode.

2.5 Fabrication of the ASCs

The asymmetrical device was assembled using the MnO_2/C/MECN and active carbon/Ni-foam electrodes separated with a polyethylene (PE) membrane. The PE membrane was pretreated and dipped in 1 M Na_2SO_4 for 10 min and assembled with the electrodes in a RS2032 battery case.

2.6 Electrochemical Measurements

The electrochemical properties of the MnO_2/C/MECN composites were assessed on a CHI 660D electrochemical workstation (Chenhua Corp., Shanghai, China) in a three electrode system. The working electrode was made of the MnO_2/C/MECN composites and a platinum wire and mercury/mercuric oxide electrode (Hg/HgO) were used as the counter and reference electrodes, respectively. The capacitive performance was determined in the electrolyte of 1.0 M Na_2SO_4 at room temperature over the potential range of -0.9−0 V at scanning rates of 10−2000mVs^{-1}.

The specific capacitance (C), energy stored (E in Wh/kg) and power delivered (P

in W/kg) by the electrode and supercapacitor cell were evaluated according to the following equations:[38]

$$C = \frac{I \times \Delta t}{m \times \Delta V} \quad (1)$$

$$C = \frac{I \times \Delta t}{S \times \Delta V} \quad (2)$$

$$E = \frac{1}{2} C (\Delta V)^2 \quad (3)$$

$$P = \frac{E}{\Delta t} \quad (4)$$

$$C = \int i dV / (s \times m \times \Delta V) \quad (5)$$

where C (F/g or F/cm^2) is the specific capacitance of the electrode based on the mass of the electroactive materials and area of the working electrode, I(A) is the current during the discharging process, Δt (s) is the discharging time, ΔV (V) is the applied potential window, S (cm^2) is the area of the working electrode, s (mV s^{-1}) is scan rate and m (g) is the mass of the electroactive materials.

2.7 Materials Characterization

The morphology, size, and structure of the materials were determined by field-emission scanning electron microscopy (FE-SEM, Hitachi S-4800, Japan), High-resolution TEM (HR-TEM, JEM-2010F), X-ray powder diffraction (XRD, Rigaku, RINR2000, Japan), micro-Raman scattering (T6400 Jobin Yvon triple monochromator, Tokyo, Japan equipped with a charge-coupled detector and an Ar laser – 633 nm).

3. RESULTS AND DISCUSSION

Figs. 2(a) and (b) depict the SEM images of the Si-MCPs providing a general

view of the morphology of the samples over a large area with a uniform structure. As shown in Figs. 2(b) and 2(c), the MECN not only retains the original 3D morphology, but also the nickel current collector with good uniformity, the inset show that the nickel current collector is composed of porous nickel with a diameter of about 50 nm. As shown in Figs. 3(a), 3(b), and 3(c), the annealed C/MECN prepared hydrothermally without depositing MnO_2 consists of stacked microspheres about 1 μm in size and possesses a porous structure.[6, 53] The elemental composition shown in Fig. 3(d) shows the presence of C, Si, and Ni with a small number of O. C comes from hydrothermal carbonization of glucose and O from colloidal carbonaceous spheres that are not reduced completely during annealing in Ar. As shown in Figs. 4(a), 4(b), and 4(c), after adding $KMnO_4$ to the second-step hydrothermal solution, the morphology of the MnO_2/C/MECN composites keeps a 3D network on the surface of the C/MECN composites, in which the hybrid MnO_2/C nano-composites on macroporous conductive network had been successfully fabricated. Fig. 4(c) discloses that the length and diameter of the MnO_2 nano-flakes are about 200 nm and 40 nm, respectively, after annealing at 60℃ for 8 h. Fig. 4(d) shows that the samples contain Mn, C, Si, Ni, and O. The ratio of Mn to O is about1:2 suggesting that the MnO_2/C hybrid composites are fabricated.

Figs. 5(a), 5(b), 5(c) and 5(d) depicts the representative TEM images of the MnO_2/C composites structure. A typical core/shell structure is shown in Fig. 5(a) and it composed of a thick core with a diameter of about 1 μm and thin shell about 40-200 nm. The HR-TEM images in Fig. 5(d) show the lattice spacing between adjacent

lattice planes of the crystalline cluster is about 0.7nm, corresponding to the distance the two (110) planes of MnO_2.

Fig. 5(e) shows the XRD patterns of MECN, MnO_2/MECN, C/MECN, and MnO_2/C/MECN. With regard to MECN, three characteristic (111), (200) and (220) diffraction peaks at 2θ = 44.8°, 52.3°, and 76.1° are identified (Ni: JCPDS card No. 01-089-7128) (marked with solid pentagram) revealing successful deposition of nickel coated Si-MCPs. After the first hydrothermal step, the Ni peaks are slightly smaller and the broad peaks at 2θ = 26° are observed (demarcated by the hollow pentagram), indicating that amorphous carbon from glucose carbonization is coated on the MECN. For MnO_2/MECN, the MnO_2 powder shows α-MnO_2 as the prominent phase, because five characteristic (200), (310), (220), (400), (301), and (002) diffraction peaks at 2θ = 22.8°, 27.7°, 31.2°, 33.0°, 41.5°, and 65.2° are identified (α-MnO_2: JCPDS card No. 44-0141). Comparing the samples before and after annealing, the relative intensity and width of the corresponding diffraction peaks from Glucose/MECN and C/MECN diminish substantially and broaden, respectively, suggesting that a large portion of the colloidal carbonaceous spheres is reduced during annealing in Ar. With regard to MnO_2/C/MECN, the new characteristic diffraction peaks at 2θ = 36.6°, 37.4°, 43.4°, 62.8°, and 63.0° corresponding to the (101), (012), (015), (110), and (113) reflection of K-Birnessite type MnO_2[37, 40, 52] are identified (MnO_2: JCPDS card No. 52-0556) (marked with diamond), suggesting that MnO_2/C/MECN is successfully synthesized. The XRD results are consistent with the SEM images in Fig. 4(c) and 4(d). Fig. 5(e) (top line) shows a dominant characteristic

(400) diffraction peak from the Si substrate at 2θ = 69.3° (marked with triangle). According to the Scherrer equation, the average crystallite size of MnO_2 is estimated to be 20-40 nm. It is believed that the MnO_2 nano-sheets and small size improve the electrochemical performance.[11] Moreover, the carbon diffraction peak diminishes significantly after the second-step of hydrothermal process.

Fig. 5(f) displays the Raman spectra of the carbon-coated MECN, which show peaks at 1350, 1580, 2700 and 2900 cm^{-1}. According to Wu et al.,[54] the Raman peaks at 1350, 1580, 2700 and 2900 cm^{-1}correspond to the D, G, 2D, and S3 bands of amorphous carbon produced from glucose hydrothermal carburization, respectively. The G band is attributed to the in-plane bond stretching of pairs of sp^2 of C atoms and the D mode is associated with disorder and defects. The results confirm that MnO_2 nano-flakes are coated uniformly on the amorphous carbon by two-steps of hydrothermal carburization.

In order to evaluate the electrochemical stability and capacitor behavior, the galvanostatic charging-discharging plots are acquired for 1,000 cycles at a constant current density of 10 mA cm^{-2} with voltage between -0.9 and 0 V. The C/ MECN composites are fabricated in glucose at different mole concentrations (0.1 M, 0.3 M, 0.5 M, 0.7 M, and 0.9 M are corresponding to sample 1, sample 2, sample 3, sample 4, and sample 5 respectively). The initial specific capacitance (Farad per unit cm^{2-}) of the MECN and C/ MECN composites at 10 mA cm^{-2} are 25, 92, 168, 186, 258, and 445 mF cm^{-2}, respectively. The initial specific capacitance increases with concentrations for C/MECN but the stability of C/MECN is poor when using a large

glucose concentration in the hydrothermal process. The stability of electrodes is important in supercapacitors.[4] Sample 3 shows capacitance retention of about 101.2% compared to the initial capacitance even after 1,000 cycles and the good cycling and rate capability can be attributed to the robust microspheres with complete reduction, better uniformity, and larger surface area. Hence, sample 3 is selected to undergo the second hydrothermal step in the 30 mM $KMnO_4$ aqueous solution at 60 ℃ for 8 h. The as-prepared MECN, MnO_2/MECN, C/MECN, and MnO_2/C/MECN composites are studied as electrode materials for supercapacitors. Fig. 6(a) shows the cyclic voltammetry curves of the different electrodes with 40 mVs^{-1}. The CV of the MECN shows that the current plateau is lower than others and that of C/MECN exhibits a quasi-rectangular loop without apparent redox peaks as the characteristic of typical EDLCs of carboneous materials. Hence, rapid diffusion of ions and better utilization of the surface is possible. The CV of the MnO_2/MECN electrode shows pseudocapacitance characteristics of MnO_2 with obvious redox peaks. Compared to other electrodes, the enhanced current plateau is observed from MnO_2/C/MECN implying that the enhanced pseudocapacitance characteristics of MnO_2 improves thetotal capacitance of MnO_2/C/MECN with swift and reversible redox peaks. The excellent CV electrochemical characteristics may be ascribed to more electron/ion paths and faster charge transport due to improved electron conductivity of MnO_2/C composites electrode,[10, 55] thereby facilitating cations adsorption and rapid ion diffusion to improve the electrochemical performance. Fig. 6(b) presents galvanostatic charging-discharging plots of different electrodes at a current density of

10 mA cm^{-2}. The MECN and C/MECN electrodes exhibit quasi-triangular charging-discharging branches indicative of a typical EDLCs capacitance and swift charging-discharging process. The discharging plots of the MnO_2/C/MECN electrode shows two voltage stages. The first stage (from 0 to -0.2 V) with a rapid voltage decrease is typical of EDLCs capacitance arising from fast discharge of accumulated electrons from the electrode surface. The other stage (from -0.2 to -0.9 V) with a longer discharge duration can be attributed to a combination of EDLCs capacitance and faradic capacitance.[11, 21] The internal resistance (IR) drops in the discharging curve of the MnO_2/MECN and MnO_2/C/MECN electrodes are -0.32 and -0.07 V, respectively, which are smaller than those of the MnO_2/MECN electrode indicating enhanced conductivity of the composite. Because the MnO_2 nanoflakes have poor conductivity, the amorphous carbon as a conductive network that covalently links to the nanosheets MnO_2 accelerates electron transfer and reduces energy loss. The specific capacitances of MECN, C/MECN, MnO_2/MECN, and MnO_2/C/MECN at 10 m A cm^{-2} are calculated to be about 62, 186, 249 and 685 mF cm^{-2}, respectively. Hence, the MnO_2/C/MECN electrode is a more promising electrode in supercapacitors.

Fig. 6(c) shows the impedance spectra and equivalent circuit obtained by complex nonlinear least square (CNLS) fitting. The impedance spectra can be fitted with the parameters shown in Fig. 6(c). The constant phase element (CPE) components are introduced in the equivalent circuit. A bulk solution resistance (R_s) is in series with a double layer capacitance (C_{dl}) at the electrolyte/electrode interface

which is in parallel with the charge transfer resistance (R_{ct}) and pseudocapacitance (CPE_p)[56]. As shown in Fig. 6(c), the combined series resistance (R_s) of the electrolyte, electrode and current collectors is 1.272 Ω, 3.144 Ω, 12.62 Ω, and 6.710 Ω for MnO_2/C/MECN, MnO_2/MECN, C/MECN and MECN, respectively. R_s of C/MECN is larger than that of other samples possibly due to that the carbon microspheres with partial hydroxyl or carboxyl groups are not completely reduced by annealing. R_s of MnO_2/C/MECN is slightly smaller than that of other samples. It may be explained by that MnO_2/C/MECN electrode have better interface surface with electrolyte than other electrodes, reducing R_s of MnO_2/C/MECN. A straight line with a slope of 45° in the low-frequency range corresponds to semi-infinite Warburg impedance resulting from the frequency dependence of the ion diffusion/transport in the electrolyte. A vertical line at very low frequencies that arising from accumulation of ions at the bottom of the pores in the electrode demonstrates better capacitive behavior without diffusion limitation, comparing to that in the MnO_2/MECN and C/MECN electrodes.

Fig. 6(d) shows that the specific capacitances of the MnO_2/C/MECN, MnO_2/MECN, C/MECN and MECN electrodes decrease gradually with increasing scanning rate. The movement of sodium ions and protons are limited because of the time constraints, and only the surface of the active materials is used to accumulate charges thus undermining electrochemical utilization of the active materials. The specific capacitance of the MnO_2/C/MECN electrode decreases from 1492 mF cm^{-2} at 2 mA cm^{-2} to 650 mF cm^{-2} at 16 mA cm^{-2} showing excellent capacitance retention. These results illustrate that MnO_2/C nano-composite hybrid on MECN enhances the

charging –discharging capability because high electrical conductivity is critical to the electrode active materials at high current densities.

Fig. 6(e) shows the capacitance retention ratio of the MnO_2/C/MECN, MnO_2/MECN, C/MECN, and MECN electrodes at 0.9 V as a function of the cycle number. The MnO_2/C/MECN electrode exhibits a specific capacitance loss rate of less than 2.1% after charging-discharging for 1000 cycles and better capacity retention than the MnO_2/MECN, C/MECN and MECN electrodes. Compared to MnO_2/C/MECN, easy detachment MnO_2 from the MnO_2/MECN electrode leads to poor adhesion and Mn dissolves in the electrolyte during ion desorption and adsorption.

Fig. 7(a) shows the cyclic voltammetry (CV) curves of the MnO_2/C/MECN electrode at different scanning rates from 10 to 2000 mV s^{-1} in 1 M Na_2SO_4. The MnO_2/C/MECN electrode shows the typical rectangular CV curves similar to the behavior of pseudo-capacitors (PCs) previously reported.[11, 44, 46, 47] The CV curves resemble a rectangle from 10 to 400mV s^{-1} and although the CV curve shape changes to lancet at a high scanning rate, the curve area increases and the symmetry of the CV curves is retained. It indicates that the reversibility of the MnO_2/C/MECN electrode reaction is not changed and the rate capability is better than those reported before.[11, 57-60]

Fig 7(b) shows the galvanostatic charging-discharging curves of the MnO_2/C/MECN composites prepared at different current densities (2, 4, 6, 8 and 16 $mAcm^{-2}$) with voltages between -0.9 V and 0 V. During the charging-discharging

process, all the curves are linear and symmetrical showing good supercapacitive behaviors at different current densities. According to equation (1), the specific capacitances of the MnO_2/C coated MECN composites are 1.491, 0.837, 0.841, 0.719, and 0.658 F cm^{-2} (497, 315, 283, 242 and 195 F g^{-1} / 74.55, 41.85, 42.05, 35.95, and 32.9 F cm^{-3}) at 2, 4, 6, 8, 16 mA cm^{-2}, respectively. With increasing current densities, the potential drops (IR-drop) become larger gradually and the specific capacitance decreases as well. The reason is that at a larger current density, many cations are adsorbed at the electrode and the concentration of cations at the interface of the electrode/electrolyte decreases. The diffusion rate of cations is slower and the concentration of cations at the electrode/electrolyte interface cannot satisfy the need and increasing polarization raised by liquid diffusion gradually plays a key role controlling the step. Therefore, as the applied potential is increases, the charges on the electrode do not increase correspondingly and the specific capacitance of the electrode is lost at a larger current density. In previous studies, the maximum specific capacitances of the MnO_2/C composite electrode were only 0.961 F cm^{-2} (323.1 F g^{-1}),[48] 225,[46] 458,[61] and 204.7 F g^{-1} [62] for an aqueous electrolyte. In comparison, the specific capacitances reported here are larger, including those of the MnO_2/MECN composites reported by ourselves before.[48] It can be attributed to the high electrical and ionic conductivity of the samples because of nano-sheet MnO_2 as well as nano-structrued MnO_2/C and MECN.

To determine the cycling stability of the MnO_2/C/MECN electrode, galvanostatic charging-discharging measurements are performed for 5000 cycles at a

current density of 20 mA cm^{-2} and potential window of -0.9 V and the results are shown in Fig. 7(c). The MnO_2/C/MECN electrode retains ~90% (0.378 F cm^{-2}/18.9 F cm^{-3}/128 F g^{-1}) of the original capacity (0.420 F cm^{-2}/ 21.0 F cm^{-3}/142 F g^{-1}) up to 5000 cycles at 20 mA cm^{-2}/ 8A g^{-1}, demonstrating good electrochemical cycle stability. The inset shows that the charging/discharging curves of the MnO_2/C/MECN electrode in potential range between -0.9 and 0 V are symmetrical and the capacitive behavior continues for 5000 cycles. The SEM image of MnO_2/C/MECN hybrid composites after 5000 cycles reveals the amount of mesoporous MnO_2 is reduced on account of Mn dissolution in the electrolyte (Figs. 4(c) and 7(c)).

EIS is conducted and the corresponding Nyquist plots are shown in Figure 7(d) to show the electrochemical behavior of the MnO_2/C/MECN electrode. The MnO_2/C/MECN electrode after the 1st cycle shows slightly smaller R_1 (1.272 Ω) and R_{ct} (0.200Ω) and steeper EIS slope in the low frequency range (R_{ct}, 1.4 Ω; R_{ct}, 0.400Ω) after 5000 cycles, illustrating that the high stability is mainly attributed to the good conductivity of the MnO_2/C nano-structure. The diameter of the arc corresponds to the Faradic charge transfer resistance (R_{ct}) at the electrode/electrolyte interface and the smaller R_{ct} of the MnO_2/C/MECN electrode (0.2 Ω) than that (0.4 Ω) after 5000 cycles illustrates mainly more rapid adsorption/desorption at the electrode/electrolyte interface. Compared to the original MnO_2/C/MECN electrode, the larger R_{ct} after 5000 cycles is due to the reduced amount of nanosheets MnO_2 arising from Mn dissolution (Fig. 7(d) for the original and after cycles). The smaller R_{ct} of the MnO_2/C/MECN electrode (0.2 and 0.4 Ω) relative to the MnO_2/MECN electrode (2.5

Ω) shows smaller Faradic charge transfer resistance due to the improved conductivity of the MECN, [48] carbon spheres, and nano-sheet MnO_2. The fact that the slope is more than 45° straight line at low frequencies representing ion diffusion resistance indicates the ideal capacitive behavior with rapid ion diffusion.

In addition to larger specific capacitance, increasing the cell voltage is another way to increase the energy density of supercapacitors. Asymmetrical supercapacitors (ASCs) can effectively make use of the voltage windows of two different electrodes to increase the operating voltage. Fig. 8(a) shows the CV curves of MnO_2/C/MECN and AC/Ni-foam single electrodes at a scan rate of 40 mV s^{-1}. Compared with the curves, CV curves of AC/Ni-foam electrodes show quasi-rectangular shapes at a potential window ranging from 0 to 1.1 V without reduction and oxidation peaks, suggesting a double electrode layer capacitive behavior. Herein, we use the prepared MnO_2/C/MECN as an anode for the ASCs and active carbon (AC)/Ni-foam as a cathode. According to the equation 5, the specific capacitance of MnO_2/C/MECN electrode and AC/Ni-foam electrode are 242 F g^{-1} and 110 F g^{-1}, respectively, and the mass rate of negative and positive materials for the asymmetrical supercapacitors is 9:20, because the mass of MnO_2/C/MECN negative electrode is fixed 3.0 mg/cm^2, and the theoretical mass of AC/Ni-foam positive electrode is about 6.6 mg/cm^2. Fig. 8(b) shows the CV curves of the MnO_2/C/MECN||AC/Ni-foam ASCs device at different scanning rates. The stable voltage window of the fabricated ASCs can be enlarged to 2.0 V and as shown in Fig. 8(b), all the CV curves exhibit the rectangular shape even at a large scanning rate of 200 mV s^{-1}.

Excellent cycling stability is crucial to high-energy supercapacitors. Fig. 8(c) shows the capacitance retention of the MnO_2/C/MECN||AC/Ni-foam ASCs device at a current density of 12 mA cm^{-2} for 5000 cycles. The device has excellent electrochemical stability with only 12.4% deterioration after 5000 cycles. The inset in Fig. 8(c) reveals no significant change of electrochemical behavioursafter 5000 cycles of charging-discharging and the outstanding cycling stability is attributed to the MECN and MnO_2 nano-sheets with good conductivity and ion diffusion. EIS is conducted and the corresponding Nyquist plots are shown in Fig. 8(d) to further assess to the electrochemical stability of the MnO_2/C/MECN||AC/Ni-foam ASCs device. The ASCs device at 12 mA cm^{-2} after the 1st cycle shows slightly smaller R_s (8.214 Ω) and R_{ct} (4.471Ω) and sharper EIS slope in the low frequency range than after cycling at 12 mA cm^{-2} for 5000 cycles. The results show that the ASCs device has high stability and electrochemical performance.

The power density (P) and energy density (E) are usually used to illustrate the electrochemical performance of supercapacitors. Fig. 8(e) shows the Ragone plots derived from the charging-discharging curve acquired at 12 mA cm^{-2} for comparison with reported values. The as-assembled MnO_2/C/MECN||active carbon/Ni-foam ASCs device delivers an energy density of 55.5 Wh kg^{-1} at a high power density of 4000 W kg^{-1}, which is higher than that of asymmetric or symmetric supercapacitors reported by other groups, for example, CVC-2||MnO_2/C (5.5 Wh kg^{-1}, 3 750W kg^{-1}),[63] SiC-N-MnO_2||active carbon (30.6 Wh kg^{-1}, 113.9 W kg^{-1}),[64] p-BC@MnO2//p-BC/N (21.0 Wh kg^{-1}, 1000.0 W kg^{-1}),[65] GHCS/MnO_2||GHCS (15.0 Wh kg^{-1}, 1000.0 W

kg^{-1}),[66] Graphene/MnO_2||CAN (23.0 Wh kg^{-1}, 4000.0 W kg^{-1}), [67] graphene||MGC (13.0 Wh kg^{-1}, 4000.0 W kg^{-1}).[68] To demonstrate the potential application, a blue light-emitting-diode (LED) is driven by our ASCs. The voltage window of the ASCs device measured is about 2 V (inset in Fig. 8(e)). The blue LED with a threshold voltage of 3.5 V can be driven by three devices in series for 100 minutes after charging at 20 mA cm^{-2} for about 30 s, confirming the large energy density of the as-assembled MnO_2/C/MECN||AC/Ni-foam ASCs in Figs. 8(e). Fig. 8(e) shows that the red LED with the threshold voltage of 1.8 V can be driven by one device for about 10 minutes after charging at 20 mA cm^{-2} for 30s.

Fig. 8(f) shows the normalized imaginary part |Q|/|S| and real part |P|/|S| versus frequencies of the MnO_2/C/MECN||AC/Ni-foam ASCs. The ASCs behaves as a pure resistance and power dissipation is 100% at high frequencies. However, it shows the capacitive behavior as the frequencies are reduced. It is well known that the variation in |Q|/|S| and |P|/|S| is opposite with frequency. The only crossing point of the two curves appears at the frequency (f_0) of ~ 125 Hz. It leads to a dielectric relaxation time constant (τ_0 being the minimum time needed to discharge with an efficiency of greater than 50%) of ~8 ms, revealing fast ion diffusion rate and shorter diffusion routes than that of MnO_2/MECN||AC/Ni-foam ASCs (τ_0, 91 ms) because of the embedded carbon and MECN.

The excellent electrochemical performance of the MnO_2/C/MECN electrode and as-assembled MnO_2/C/MECN||AC/Ni-foam ASCs can be attributed to the following factors: (1) The patterned and well-ordered MnO_2/C nanoflakes hybrid electro-active

materials have a lot of micro/nano-scale tunnels for adsorption and desorption of electrolyte sodium ions in and out of the MnO_2 to reduce the diffusion paths of electrolyte ions a large scanning rates and enhance surface utilization of the MnO_2; (2) The uniform carbon microspheres not only act as a support for the MnO_2 nanoflakes, but also play a key role in providing good conductivity of the MnO_2/C hybrid to facilitate Faradic charge transfer and increase the contact area between the carbon microspheres and MnO_2 nanoflakes; (3) The 3D MECN in the electrode leads to high electrical conductivity, good mechanical properties, and good electrochemical stability, thus improving the stability of the MnO_2/C/MECN electrode at large scanning rates and shortening the electron transfer path; (4) The large surface area and pore volume in the 3D MECN are favorable to the formation of big EDLCs and alleviating structural destruction induced by volume expansion under high charging/discharging cycling, thus enabling electrolyte ions to reach deeply into the electrode materials. This accelerates the highly reversible faradic reaction between the Na_2SO_4 electrolyte and MnO_2/C/MECN electrode and enhances the cycling characteristics of the electrode as well. The encouraging results obtained from the MnO_2/C/MECN electrode and MnO_2/C/MECN||AC/Ni-foam ASCs suggest large commercial potential in energy storage.

4. Conclusion

MnO_2/C/MECN composite electrodes without binders are fabricated by a two-step hydrothermal process. The nanosheet MnO_2-coated MECN conductive

network result in fast ion transport and good electrical conductivity producing pseudocapacitance and double-layer capacitance in the hybrid electrode. The MnO_2/C/MECN nanocomposites are excellent supercapacitor electrodes delivering a high capacitance of 497 F/g at 1 A/g for 1 cm^2 samples and excellent long-term cycling stability for over 5,000 cycles in 1 M Na_2SO_4. The MnO_2/C/MECN||AC/Ni-foam ASCs device delivers an energy density of 0.50 mW h cm^{-3}/55.5 Wh kg^{-1} at a high power density of 4000 W kg^{-1}. The high-performance MnO_2/carbon composite materials have large potential in electrochemical energy storage applications.

Conflict of interest: The authors declare no competing financial interest.

Acknowledgments:

This work was jointly supported by Shanghai Pujiang Program (No. 14PJ1403600), Shanghai Fundamental Key Project (No. 11JC1403700), National Naltural Science Foundation of China (No. 61176108), PCSIRT, Research Innovation Foundation of ECNU (No. 78210245), Huaian Applied Research (No. HAG2014034) and City University of Hong Kong Applied Research Grant (ARG) No. 9667104.

REFERENCES AND NOTES

1. J. Chmiola, C. Largeot, P.-L. Taberna, P. Simon and Y. Gogotsi, *Science*, 2010, **328**, 480-483.

2. D. Pech, M. Brunet, H. Durou, P. Huang, V. Mochalin, Y. Gogotsi, P.-L. Taberna and P. Simon, *Nature nanotechnology*, 2010, **5**, 651-654.

3. X. Yang, C. Cheng, Y. Wang, L. Qiu and D. Li, *Science*, 2013, **341**, 534-537.

4. H. Kim, M. E. Fortunato, H. Xu, J. H. Bang and K. S. Suslick, *The Journal of Physical Chemistry C*, 2011, **115**, 20481-20486.

5. B. E. Conway, *Journal of the Electrochemical Society*, 1991, **138**, 1539-1548.

6. L. L. Zhang and X. Zhao, *Chemical Society Reviews*, 2009, **38**, 2520-2531.

7. H. Y. Lee and J. B. Goodenough, *Journal of Solid State Chemistry*, 1999, **144**, 220-223.

8. X. Wang, J. Ding, S. Yao, X. Wu, Q. Feng, Z. Wang and B. Geng, *Journal of Materials Chemistry A*, 2014, **2**, 15958-15963.

9. L. Zhang, F. Zhang, X. Yang, K. Leng, Y. Huang and Y. Chen, *small*, 2013, **9**, 1342-1347.

10. H. Xia, Y. Wang, J. Lin and L. Lu, *Nanoscale research letters*, 2012, **7**, 1-10.

11. M. Liu, L. Gan, W. Xiong, Z. Xu, D. Zhu and L. Chen, *Journal of Materials Chemistry A*, 2014, **2**, 2555-2562.

12. Y. Zhao, J. Liu, Y. Hu, H. Cheng, C. Hu, C. Jiang, L. Jiang, A. Cao and L. Qu, *Adv. Mater.*, 2013, **25**, 591-595.

13. J. M. D'Arcy, M. F. El-Kady, P. P. Khine, L. Zhang, S. H. Lee, N. R. Davis, D. S. Liu, M. T. Yeung, S. Y. Kim and C. L. Turner, *ACS nano*, 2014, **8**, 1500-1510.

14. L. Gu, Y. Wang, R. Lu, W. Wang, X. Peng and J. Sha, *Journal of Power*

Sources, 2015, **273**, 479-485.

15. M. Liu, W. W. Tjiu, J. Pan, C. Zhang, W. Gao and T. Liu, *Nanoscale*, 2014, **6**, 4233-4242.

16. P. Vialat, C. Mousty, C. Taviot-Gueho, G. Renaudin, H. Martinez, J. C. Dupin, E. Elkaim and F. Leroux, *Advanced Functional Materials*, 2014, **24**, 4831-4842.

17. X. Xia, J. Tu, Y. Zhang, X. Wang, C. Gu, X.-b. Zhao and H. J. Fan, *ACS nano*, 2012, **6**, 5531-5538.

18. H. Jiang, J. Ma and C. Li, *Adv. Mater.*, 2012, **24**, 4197-4202.

19. X. Lang, A. Hirata, T. Fujita and M. Chen, *Nature Nanotechnology*, 2011, **6**, 232-236.

20. X.-C. Dong, H. Xu, X.-W. Wang, Y.-X. Huang, M. B. Chan-Park, H. Zhang, L.-H. Wang, W. Huang and P. Chen, *ACS nano*, 2012, **6**, 3206-3213.

21. J. W. Long, M. B. Sassin, A. E. Fischer, D. R. Rolison, A. N. Mansour, V. S. Johnson, P. E. Stallworth and S. G. Greenbaum, *The Journal of Physical Chemistry C*, 2009, **113**, 17595-17598.

22. H. Huang and X. Wang, *Nanoscale*, 2011, **3**, 3185-3191.

23. Y. Hou, Y. Cheng, T. Hobson and J. Liu, *Nano letters*, 2010, **10**, 2727-2733.

24. T. Wang, Z. Peng, Y. Wang, J. Tang and G. Zheng, *Scientific reports*, 2013, **3**.

25. Y. Xia, Z. Xiao, X. Dou, H. Huang, X. Lu, R. Yan, Y. Gan, W. Zhu, J. Tu and W. Zhang, *ACS nano*, 2013, **7**, 7083-7092.

26. B. Wang, J. Park, C. Wang, H. Ahn and G. Wang, *Electrochimica Acta*, 2010,

55, 6812-6817.

27. C.-C. Hu, Y.-T. Wu and K.-H. Chang, *Chemistry of Materials*, 2008, **20**, 2890-2894.

28. A. Facile, *Chemistry of Materials*, 2012, **24**, 1158-1164.

29. J. W. Lee, A. S. Hall, J.-D. Kim and T. E. Mallouk, *Chemistry of Materials*, 2012, **24**, 1158-1164.

30. R. Zhou, C. Meng, F. Zhu, Q. Li, C. Liu, S. Fan and K. Jiang, *Nanotechnology*, 2010, **21**, 345701.

31. X. Wang, L. Liu, X. Wang, L. Yi, C. Hu and X. Zhang, *Materials Science and Engineering: B*, 2011, **176**, 1232-1238.

32. X. Tang, Z.-h. Liu, C. Zhang, Z. Yang and Z. Wang, *Journal of Power Sources*, 2009, **193**, 939-943.

33. H.-S. Kim, J. B. Cook, S. H. Tolbert and B. Dunn, *Journal of The Electrochemical Society*, 2015, **162**, A5083-A5090.

34. Q. Qu, P. Zhang, B. Wang, Y. Chen, S. Tian, Y. Wu and R. Holze, *The Journal of Physical Chemistry C*, 2009, **113**, 14020-14027.

35. X. Lu, T. Zhai, X. Zhang, Y. Shen, L. Yuan, B. Hu, L. Gong, J. Chen, Y. Gao and J. Zhou, *Adv. Mater.*, 2012, **24**, 938-944.

36. D. Zheng, S. Sun, W. Fan, H. Yu, C. Fan, G. Cao, Z. Yin and X. Song, *The Journal of Physical Chemistry B*, 2005, **109**, 16439-16443.

37. R. Ma, Y. Bando, L. Zhang and T. Sasaki, *Adv. Mater.*, 2004, **16**, 918-922.

38. H. Jiang, C. Li, T. Sun and J. Ma, *Nanoscale*, 2012, **4**, 807-812.

39. P. Yu, X. Zhang, D. Wang, L. Wang and Y. Ma, *Crystal Growth and Design*, 2008, **9**, 528-533.

40. T. Brousse, M. Toupin, R. Dugas, L. Athouël, O. Crosnier and D. Bélanger, *Journal of The Electrochemical Society*, 2006, **153**, A2171-A2180.

41. A. E. Fischer, K. A. Pettigrew, D. R. Rolison, R. M. Stroud and J. W. Long, *Nano Letters*, 2007, **7**, 281-286.

42. Y. He, W. Chen, X. Li, Z. Zhang, J. Fu, C. Zhao and E. Xie, *ACS nano*, 2012, **7**, 174-182.

43. X. Zhang, X. Sun, H. Zhang, D. Zhang and Y. Ma, *Materials Chemistry and Physics*, 2012, **137**, 290-296.

44. S.-B. Ma, K.-W. Nam, W.-S. Yoon, X.-Q. Yang, K.-Y. Ahn, K.-H. Oh and K.-B. Kim, *Journal of Power Sources*, 2008, **178**, 483-489.

45. S.-W. Kim, T. H. Han, J. Kim, H. Gwon, H.-S. Moon, S.-W. Kang, S. O. Kim and K. Kang, *ACS nano*, 2009, **3**, 1085-1090.

46. X. Zhang, J. Ma, W. Yang, Z. Gao, J. Wang, Q. Liu, J. Liu and X. Jing, *CrystEngComm*, 2014, **16**, 4016-4022.

47. Z. Li, Q. Li, Y. Fang, H. Wang, Y. Li and X. Wang, *Journal of Materials Chemistry*, 2011, **21**, 17185-17192.

48. Y. Xu, S. Xu, M. Li, Y. Zhu, L. Wang and P. K. Chu, *Materials Letters*, 2014, **126**, 116-118.

49. M. Li, S. Xu, T. Liu, F. Wang, P. Yang, L. Wang and P. K. Chu, *Journal of Materials Chemistry A*, 2013, **1**, 532-540.

50. B. Hu, K. Wang, L. Wu, S. H. Yu, M. Antonietti and M. M. Titirici, *Adv. Mater.*, 2010, **22**, 813-828.

51. B. Hu, X. Qin, A. M. Asiri, K. A. Alamry, A. O. Al-Youbi and X. Sun, *Electrochimica Acta*, 2013, **100**, 24-28.

52. L. Athouël, F. Moser, R. Dugas, O. Crosnier, D. Bélanger and T. Brousse, *The Journal of Physical Chemistry C*, 2008, **112**, 7270-7277.

53. S. Dutta, A. Bhaumik and K. C.-W. Wu, *Energy & Environmental Science*, 2014, **7**, 3574-3592.

54. J.-B. Wu, X. Zhang, M. Ijäs, W.-P. Han, X.-F. Qiao, X.-L. Li, D.-S. Jiang, A. C. Ferrari and P.-H. Tan, *Nature communications*, 2014, **5**.

55. X. Ma, M. Liu, L. Gan, Y. Zhao and L. Chen, *Journal of Solid State Electrochemistry*, 2013, **17**, 2293-2301.

56. Z. Gao, F. Wang, J. Chang, D. Wu, X. Wang, X. Wang, F. Xu, S. Gao and K. Jiang, *Electrochimica Acta*, 2014, **133**, 325-334.

57. H.-l. Fan, F. Ran, X.-x. Zhang, H.-m. Song, X.-q. Niu, L.-b. Kong and L. Kang, *Nano-Micro Letters*, 1-9.

58. S.-L. Chou, J.-Z. Wang, S.-Y. Chew, H.-K. Liu and S.-X. Dou, *Electrochemistry Communications*, 2008, **10**, 1724-1727.

59. G.-Y. Zhao, C.-L. Xu and H.-L. Li, *Journal of power sources*, 2007, **163**, 1132-1136.

60. X. Wang, X. Wang, W. Huang, P. Sebastian and S. Gamboa, *Journal of Power Sources*, 2005, **140**, 211-215.

61. R. K. Sharma, H.-S. Oh, Y.-G. Shul and H. Kim, *Journal of Power Sources*, 2007, **173**, 1024-1028.

62. J. Yang, L. Zou, H. Song and Z. Hao, *Desalination*, 2011, **276**, 199-206.

63. Z. Chen, Y. Qin, D. Weng, Q. Xiao, Y. Peng, X. Wang, H. Li, F. Wei and Y. Lu, *Advanced Functional Materials*, 2009, **19**, 3420-3426.

64. M. Kim and J. Kim, *Physical Chemistry Chemical Physics*, 2014, **16**, 11323-11336.

65. L.-F. Chen, Z.-H. Huang, H.-W. Liang, Q.-F. Guan and S.-H. Yu, *Adv. Mater.*, 2013, **25**, 4746-4752.

66. Z. Lei, J. Zhang and X. Zhao, *Journal of Materials Chemistry*, 2012, **22**, 153-160.

67. Z. Fan, J. Yan, T. Wei, L. Zhi, G. Ning, T. Li and F. Wei, *Advanced Functional Materials*, 2011, **21**, 2366-2375.

68. Z.-S. Wu, W. Ren, D.-W. Wang, F. Li, B. Liu and H.-M. Cheng, *ACS nano*, 2010, **4**, 5835-5842.

69. S. Xu, F. Wang, L. Mai, L. Wang and P. K. Chu, *Electrochimica Acta*, 2013, **90**, 344-349.

70. Lianwei wang, Cheng Liang, Yiping Zhu and Shaohui Xu, Chinese Patent (in pending), No.2015101249340.

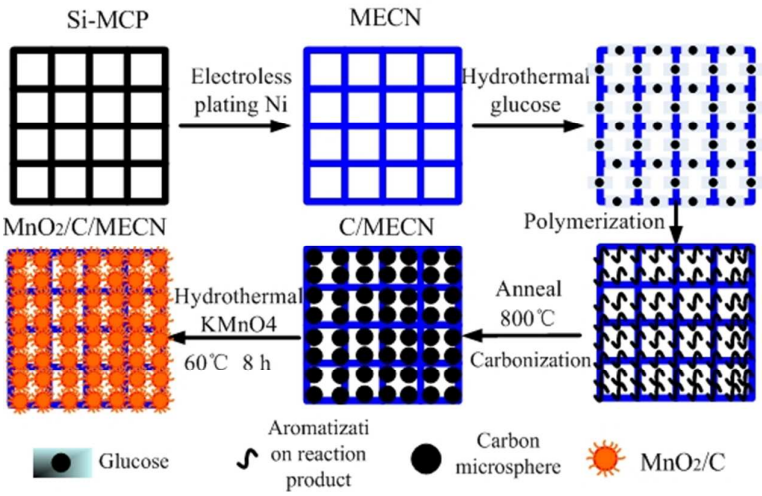

Fig. 1. Illustration of the procedures to prepare the MnO_2/C/MECN hybrid composites.

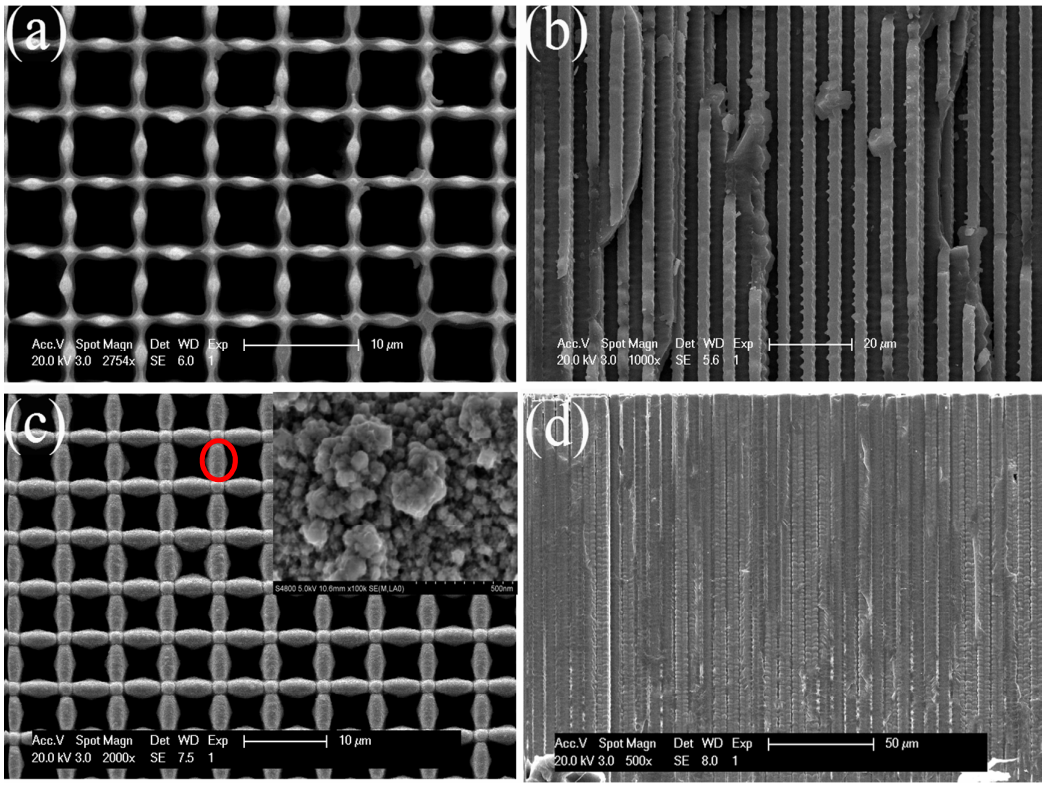

Fig. 2. SEM images: (a) Top surface of the Si-MCPs; (b) Cross-sectional morphology of the Si-MCPs; (c) Top surface of the MECN with inset showing the magnification of a select area of MECN; (d) Cross-sectional morphology of the MECN.

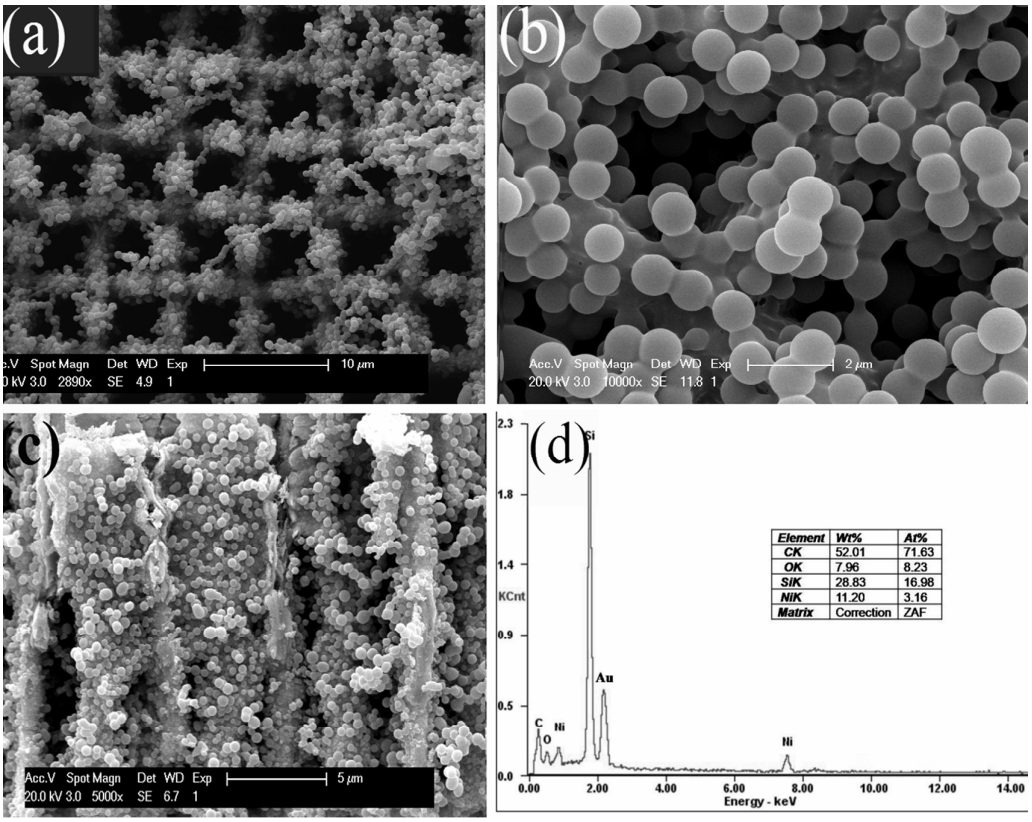

Fig. 3. (a) Top-view of the C/MECN hybrid composites; (b) Magnified SEM image of (a); (c) Cross-sectional SEM of the C/MECN hybrid composites; (d) Corresponding EDS of the C/ MECN composites with inset showing the elemental composition.

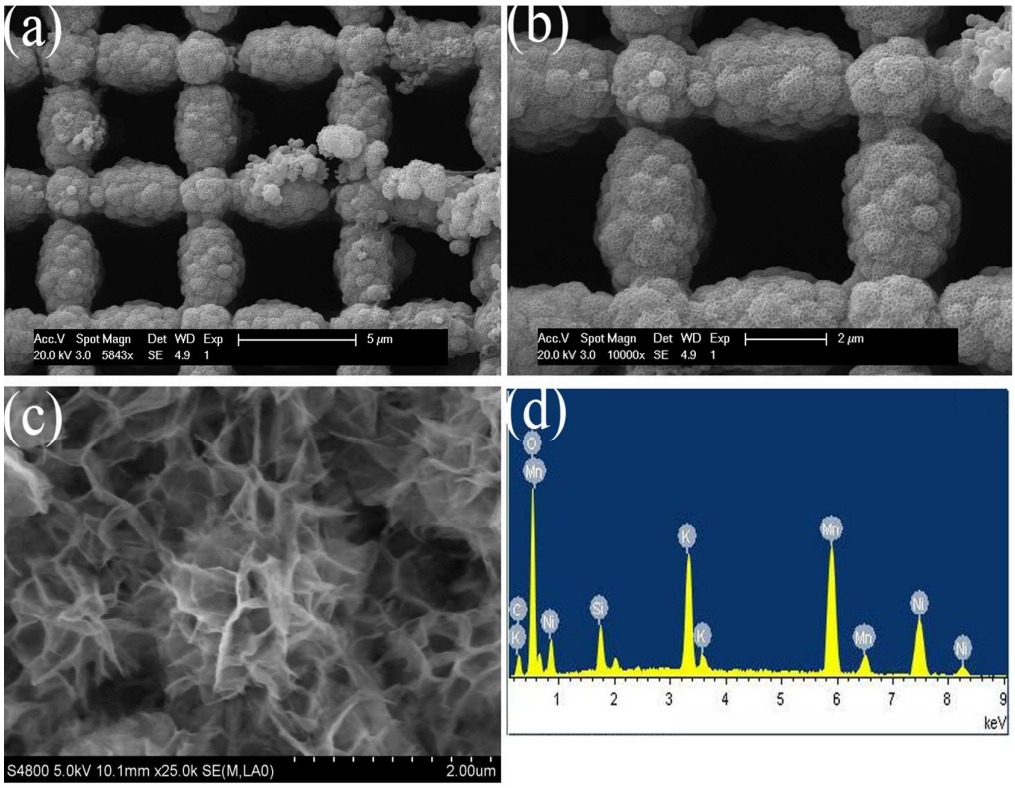

Fig. 4. SEM images of the MnO_2/C/MECN: (a) Top surface; (b) Magnified SEM image of (a); (c) Cross-sectional morphology; (d) Corresponding EDS spectrum.

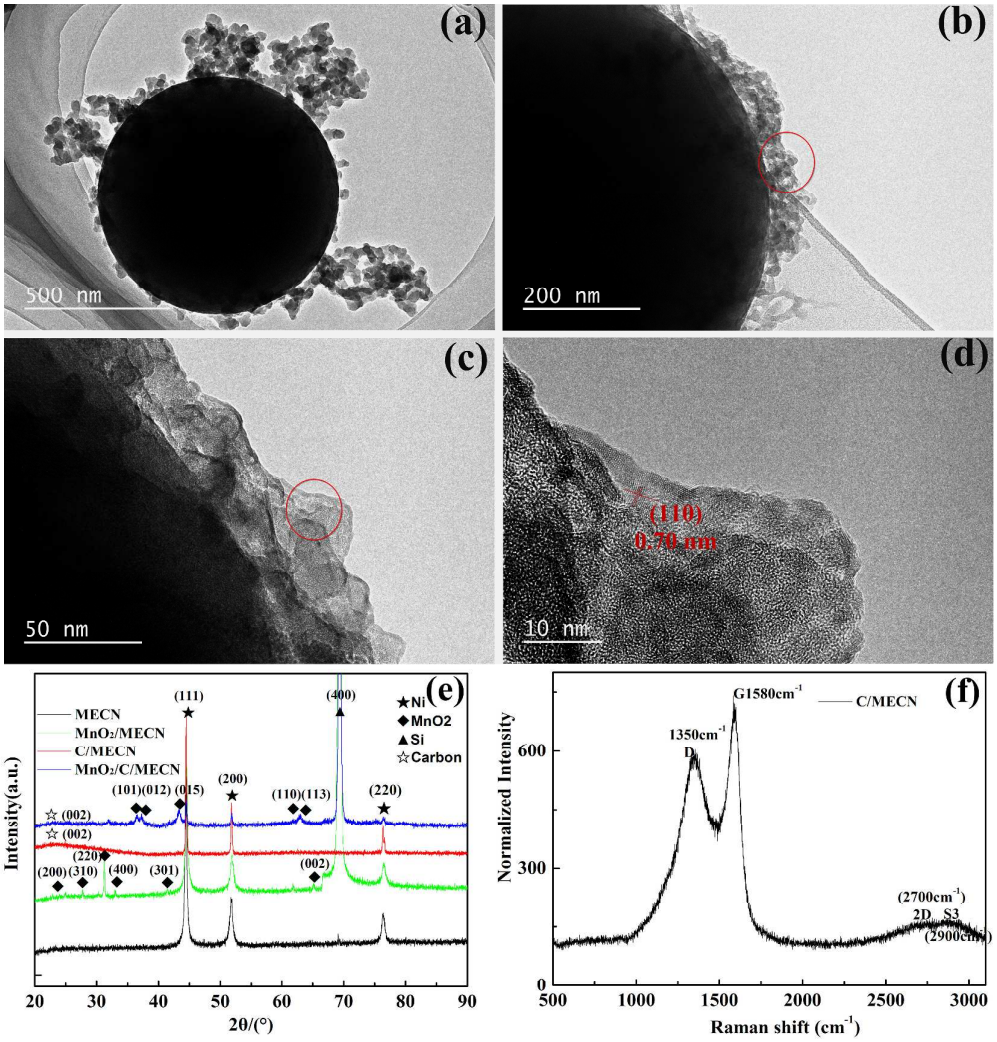

Fig. 5. TEM images, XRD patterns and Raman spectra of the MnO_2/C/MECN hybrid composites: (a) TEM images of MnO_2/C with core-shell structure at low magnification; (b) MnO_2 on the shell of carbon spheres; (c) High magnification of a selected area of part b; (d) Representative HR-TEM of nanosheet; (e) XRD patterns of MnO_2/ C/MECN (blue line) with diamond on the bottom representing MECN (black line) and in the middle C/MECN annealed (red line) and MnO_2/ C/MECN (green line); (f) Raman spectra of C/MECN.

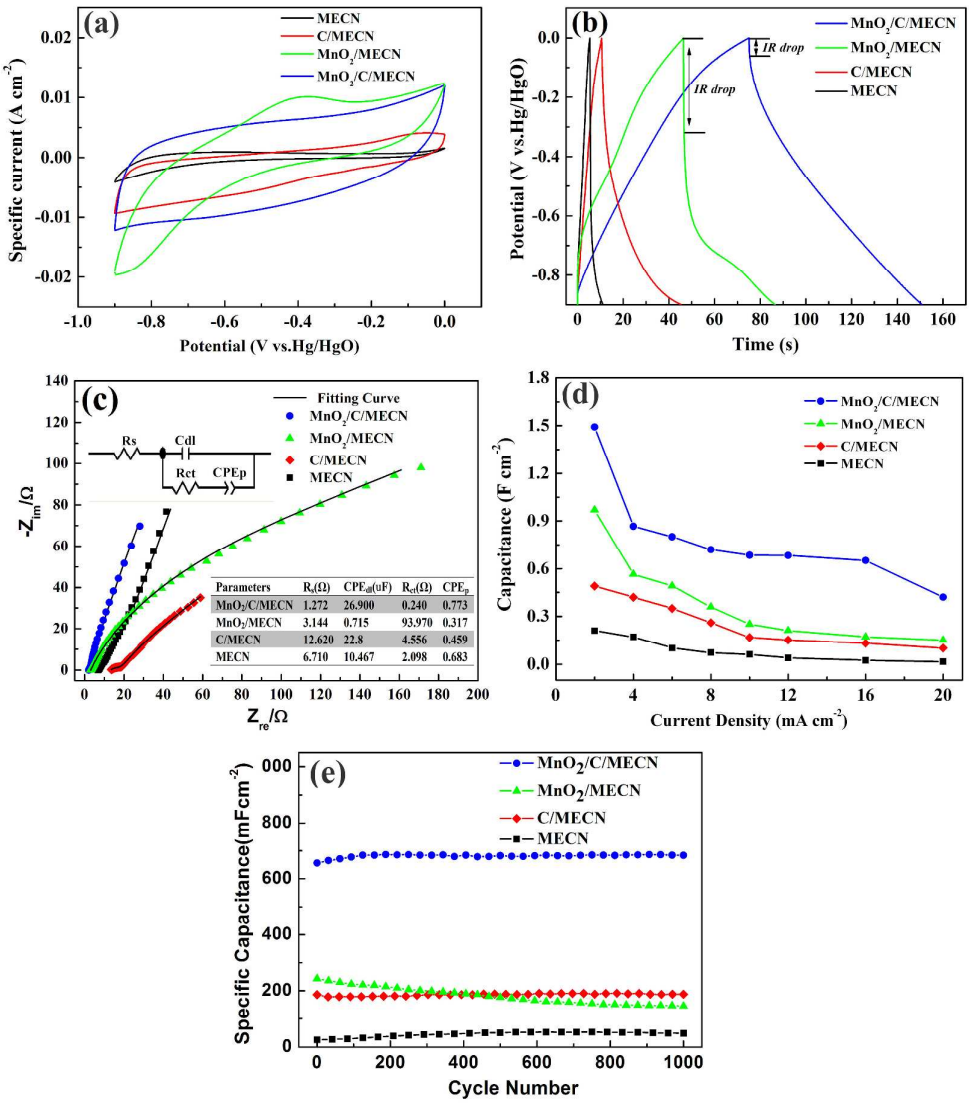

Fig. 6. (a) CVs of the MECN, C/MECN, MnO_2/MECN and MnO_2/C/MECN electrodes at a scanning rate of 40 mV s^{-1} in 1 M Na_2SO_4 solution; (b) Galvanostatic charging-discharging curves of the MECN, C/MECN, MnO_2/MECN, and MnO_2/C/MECN electrodes in the three-electrode mode at a current density of 10 mA cm^{-2}; (c) Nyquist plots and corresponding simulation results of the MECN, C/MECN, MnO_2/MECN, and MnO_2/C/MECN electrodes. The inset is the equivalent circuit for fitting the equivalent circuit; (d) Specific capacitances of the MnO_2/C/MECN, MnO_2/MECN, C/MECN, and MECN electrodes with increasing scanning rates in 1 M

Na_2SO_4 aqueous solution at a potential window of 0.9 V; (e) Cycling stability of the MnO_2/C/MECN, MnO_2/MECN, C/MECN, and MECN electrodes at a current density of 10 m A cm^{-2}.

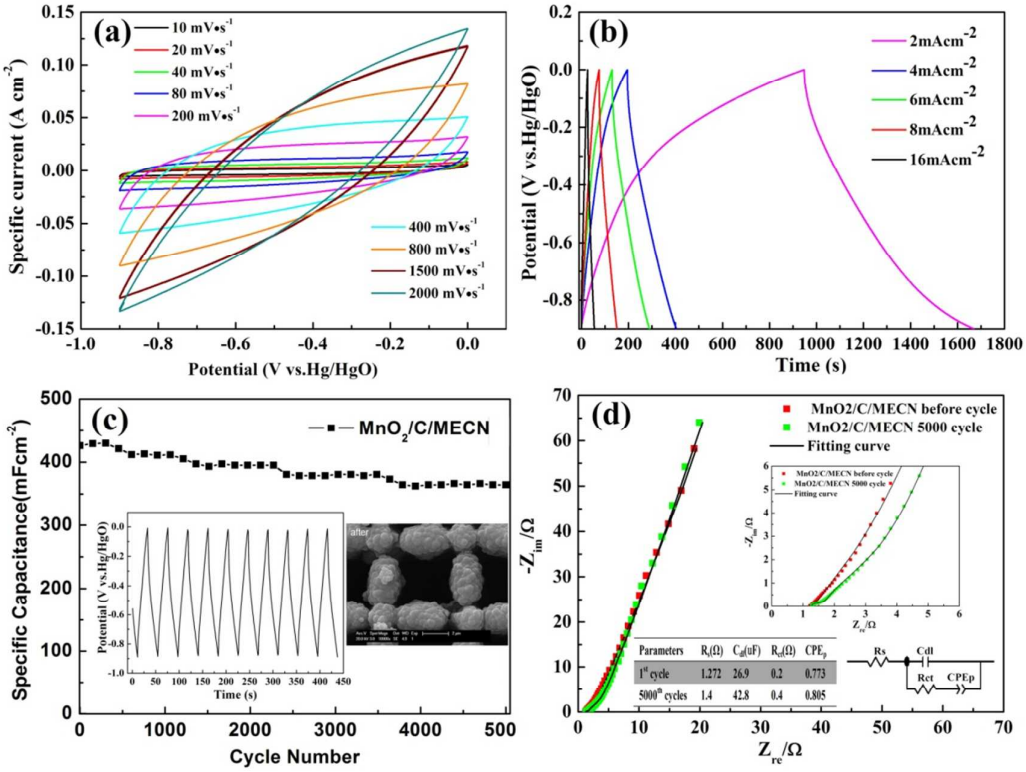

Fig. 7. (a) CVs of the MnO_2/C/MECN electrodes at different scanning rates in 1 M Na_2SO_4 solution.; (b) Galvanostatic charging-discharging curves of the MnO_2/C/MECN electrodes in the three-electrode mode at different current densities; (c) Cycling stability of the MnO2/C/MECN electrodes prepared hydrothermally in 30 mM $KMnO_4$ for 8 h at a current density of 20 mA cm^{-2}. The inset shows the charging/discharging curves of the the MnO_2/C/MECN electrodes in the potential range between -0.9 and 0 V and SEM image of the MnO_2/C/ MECN hybrid composites after 5,000 cycles; (d) Nyquist plots of the as-prepared MnO_2/C/MECN electrode. The inset is the equivalent circuit for fitting of the important parameters in the equivalent circuit and magnified high frequency.

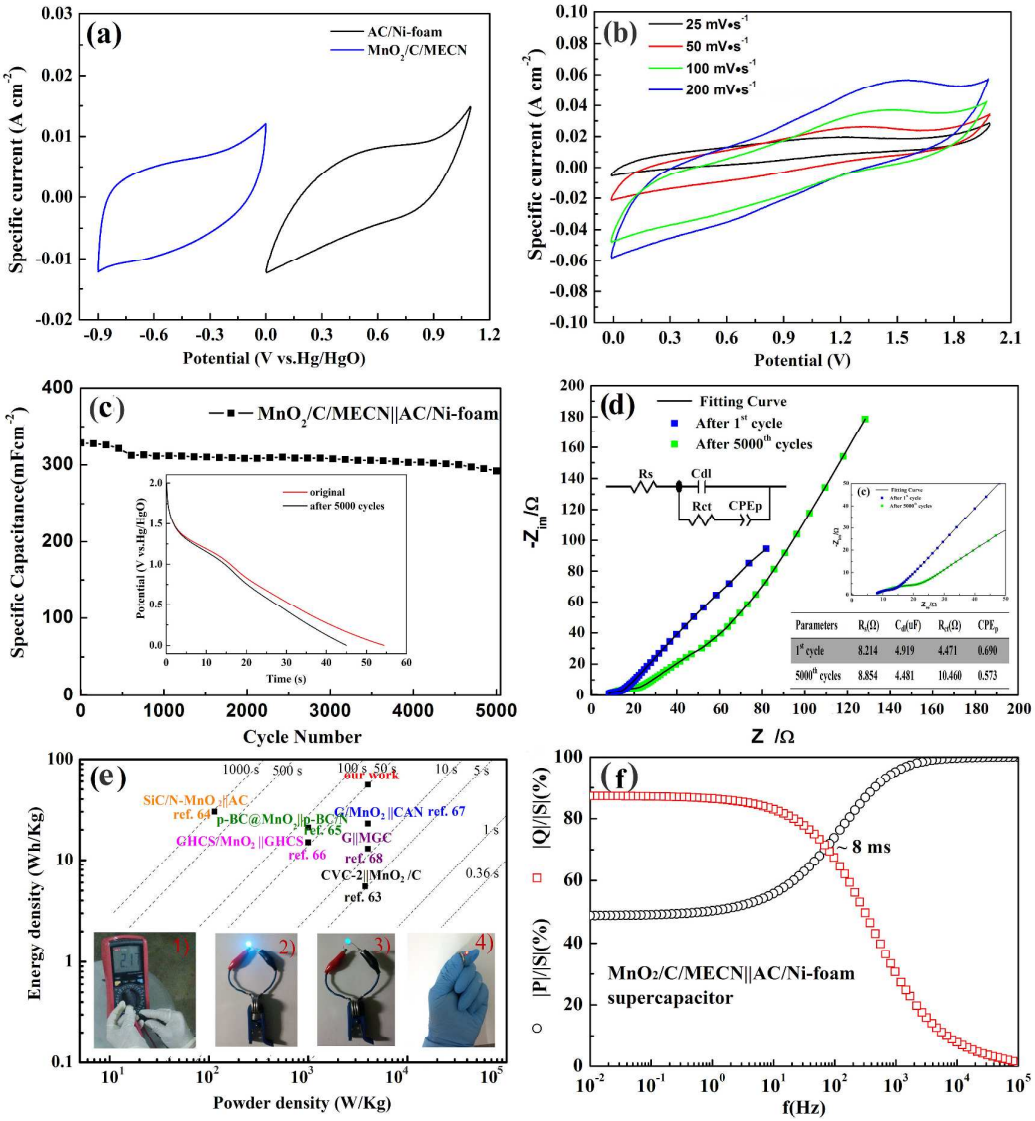

Fig. 8. (a) The CV curves of MnO_2/C/MECN and AC/Ni-foam single electrodes at a scan rate of 40 mV s^{-1}; (b) CV curves of the as-assembled MnO_2/C/MECN||AC/Ni-foam ASCs acquired at a different scanning rates; (c) Cycling performance of the MnO_2/C/MECN||AC/Ni-foam ASCs devices at a current density of 12 mA cm^{-1} for 5,000 cycles. The inset shows the charging-discharging curves in the beginning and after 5,000 cycles; (d) Nyquist plots and corresponding simulated results of the three electrodes. The inset is the equivalent circuit for fitting the equivalent circuit and magnified high frequency; (e) Ragone plot of the

as-assembled MnO_2/C/MECN||AC/Ni-foam ASCs. The values reported from other supercapacitors are shown for comparison. The insets show the voltage window by a voltmeter, blue LED in the beginning and after 100 minutes, and red LED with the threshold voltage of 1.8V; (f) Normalized reactive power |Q|/|S| and active power |P|/|S| versus frequency plots of MnO_2/C/MECN supercapacitor.

Graphical Abstract:

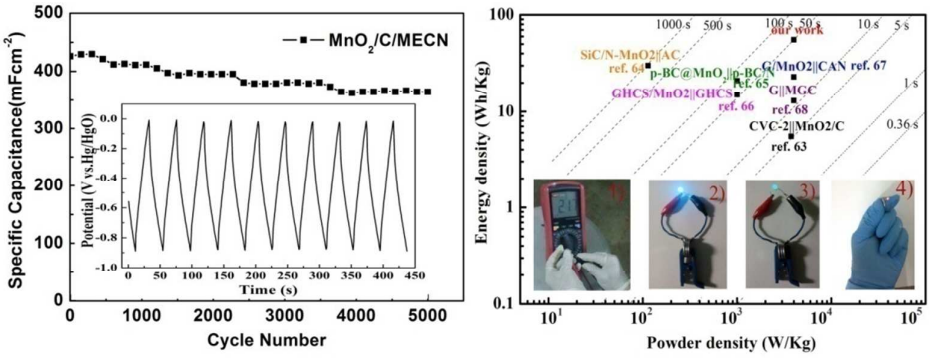

Hybrid MnO_2/C nano-composites are formed on a macroporous electrically conductive network (MECN) electro-active electrode. The relationship among the molarity, reaction time, morphology, and formation mechanism of the MnO_2/C/MECN electrode and faradic behavior are studied. After the hydrothermal reaction in a 0.5 M glucose aqueous solution and redox reaction of 30 mM $KMnO_4$ solution for 8 h, the MnO_2/C/MECN electrodes show area capacitance of 1.491 F cm^{-2}/volumetric capacitance of 74.5 F cm^{-3}/specific capacitance of 497 F g^{-1} at 2 mA cm^{-2} in the 1 M Na_2SO_4 electrolyte with a retention ratio of ~90% after 5,000 cycles. The MnO_2/C/MECN electrode as the negative electrode and active carbon/Ni-foam (AC/NF) as the positive electrode are packaged in an assembly with CR2032 batteries. The asymmetrical supercapacitors (ASCs) device delivers a high energy density of 0.50 mW h cm^{-3} (55.5 Wh kg^{-1} at a power density of 4000 W kg^{-1}) with 87.6% retention of the specific capacitance after 5,000 cycles. After charging each hybrid device for 30 s, three devices in series can power a blue LED for about 100 minutes.